Numerical Analysis of Kidney Stone Fragmentation by Short Pulse Impingement*

Sandro MIHRADI**, Hiroomi HOMMA*** and Yasuhiro KANTO**

In this work, numerical analyses are performed to study the behavior of stresses generated inside a kidney stone by direct pulse impingement during extracorporeal shock wave lithotripsy (ESWL), which leads to fragmentation of the stone. LS-DYNA, an explicit Finite Element code for non-linear dynamic analysis is employed to model the problems. Effects of pulse duration and acoustic property of the stone on stress field evolution inside the stone are studied for the pulse duration of 0.5 to 5.0 μs and two acoustic impedances of actual kidney stones. The use of double shock wave sources to fragment the kidney stone is also considered in this paper. The effectiveness of this method for the kidney stone fragmentation is confirmed. Finally, the numerical analysis for the stone fragmentation is well compared with experimental results to confirm that the numerical analyses in this work provide reasonable results.

Key Words: ESWL, Kidney Stone, Short Pulse Wave, Dual Pulse Impingement

1. Introduction

In the past two decades, extracorporeal shock wave lithotripsy (ESWL) has been extensively used to treat kidney stone disease, where thousands of focused shock waves are transmitted during the treatment in order to fragment the stone into reasonably small pieces, which then could be released naturally. Despite its success, kidney tissue injuries have been widely reported and the fragmentation mechanism of the kidney stone is not well understood yet.

Even though several mechanisms of kidney stone fragmentation have been proposed, a complete agreement on how lithotripter shock wave (LSW) breaks the stone has not been reached yet. There is still big argument on relative contributions of direct stress waves and cavitation to the fracture processes[1]. In the typical clinical lithotripter source (electro-hydraulic generator), focused shock waves are generated and targeted onto the stone, which is located at second focal point of the lithotripter. Pressure measurement at the focal point indicates a steep compressive front with duration of up to 1 μs and magnitude of around 40 MPa, followed by negative pressure of 10 MPa. The entire pulse configuration has duration of 4 μs[2]. In the cavitation hypothesis, the negative pressure tail of ESWL may be responsible for the stone damage since it can excite the growth of cavitation nuclei and expand them to larger size bubbles, which then may collapse the stone surface[3]. Upon collapse, highly localized stresses cause surface pitting and crack propagation that may catastrophically fragment the stone. On the other hand, the hypothesis of direct stress wave contribution proposes that high compressive stresses may be responsible for the erosion on the front surface of the stone, while at the back surface, spalling failure may occur due to the reflected tensile wave[4].

Three different modes of stone damages during ESWL have been identified so far. Besides the surface erosion on the front surface of the stone facing the incident shock wave, other damage modes are spalling at the back surface and delamination along the boundary of dissimilar stone components[5],[6]. To shed light on the contribution of direct stress wave toward the stone fragmentation, understanding of stress field evolution inside solids subjected to a lithotripter shock wave is needed. Clarification of stone fragmentation mechanisms must be made based on mechanics of fracture. Such approach will pro-

* Received 26th January, 2004 (No. 04-4038)

** Department of Mechanical Engineering, Toyohashi University of Technology, 1–1 Hibarigaoka, Tempaku-cho, Toyohashi, Aichi 441–8580, Japan.
E-mail: sandro@frp.mech.tut.ac.jp

*** International Cooperation Center for Engineering Education Development, Toyohashi University of Technology, 1–1 Hibarigaoka, Tempaku-cho, Toyohashi, Aichi 441–8580, Japan. E-mail: homma@icceed.tut.ac.jp

vide fundamental knowledge that can be used to improve lithotripter technology and treatment strategy to facilitate fracture processes of stone and at the same time to reduce tissue injury.

In this paper, a numerical model is presented to compute stress field evolution inside the stone subjected to short pulse loading. Then, the effects of pulse duration and acoustic property of the stone on the stress fields generated inside the stone are investigated. Use of dual pulse impingement is also introduced to study its effectiveness for patient-friendly stone fragmentation in this work. The idea is based on the assumption that this application will increase the stress level inside the stone, so that the stone fragmentation will be effectively brought. In this model, the effect of source combination on the stress responses inside the stone will also be investigated by changing the angle between two pulse sources. Finally, a simple kidney stone fragmentation model is constructed to estimate the fracture pattern in the stone subjected to direct pulse impingement. The estimated fracture pattern will be compared with the experimental results by Xi et al.[7], which demonstrate the damage pattern of cylindrical stone with various diameters when the stones are exposed to the LSW.

2. Modeling

LS-DYNA, an explicit Finite Element code for nonlinear dynamic analysis is utilized to model the problem. The software has special features to treat contact interfaces of structure inside a continuum model. Moreover, an artificial bulk viscosity has also been taken into account to treat the shock wave propagation in the water.

2.1 Physical aspect in lithotripter field

In an electro-hydraulic lithotripter, as depicted in Fig. 1, a spark generates an expanding spherical wave, which then redirected by ellipsoidal reflector. As the reflected wave of the pulse converges toward the second focal point of the reflector, its amplitude is steeply raised into a shock wave. Cleveland et al. reported that a 6 dB beam width of pressure was measured near the focal region of Dornier HM3 (electro-hydraulic) lithotripter[2]. The focal region defined as the full-width and half-maximum of the peak positive pressure was 60 mm long in the axial direction and 10 mm wide in the lateral direction. This evidence shows that actually the shock wave does not converge into a point, but a small region. This fact also demonstrates that infinite amplitude is not realized in the real fluid due to nonlinearity.

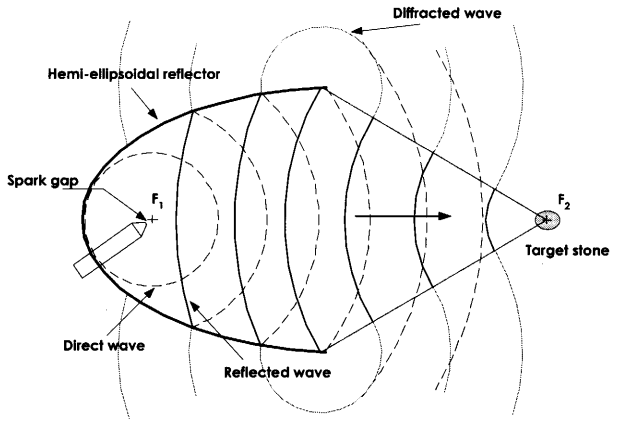

Fig. 1 Schematic diagram of an electro-hydraulic lithotripter

Because the area of interest is limited only to the area where the stone is located (i.e. focal region), and kidney stones are typically of the same dimension with focal region width, the incident wave front onto the stone can be considered as a plane wave. This plane wave impacts the stone and propagates through the stone as a compressive stress wave.

2.2 Stone properties

Renal calculus properties widely vary and strongly depend on their chemical compositions. The range of physical properties of various compositions of renal calculi is presented in Table 1[8]. Renal calculi have acoustic and mechanical properties distinctly different from those of the surrounding media inside the kidney; e.g., urine or kidney tissue as shown in Table 2[9]. The acoustic properties indicate how much incident shock wave energy is transmitted from one medium to another or is reflected at the surface boundary. These properties also describe wave propagation characteristics in a specific medium.

In the numerical model, two types of kidney stones are used. They are calcium oxalate and calcium phosphate stones. The properties of these stones are measured

Table 1 Range of physical properties of renal calculi

	Renal Calculi (combined data of Ca Oxalate, Ca, Apa, and Mg Amn Phos)
Wave Speed (m/s)	1,875 ~ 3390
Density (kg/m^3)	970 ~ 2110
Impedance (kg/m^2.s)	2.82 ~ 5.93 x 10^6
Material Failure Strength (MPa)	2.0 ~ 17.6 in compression 0.1 ~ 3.4 in tension
Young's Modulus (GPa)	4.74 ~ 17.03

Table 2 Comparison of acoustic properties of water and human tissue

Material	Density (kg/m^3)	Sound speed (m/s)	Acoustic impedance (kg/m^2 .s)
Water	1000	1500	1.5x10^6
Kidney, liver, muscle, blood	1050	1580	1.65x10^6
Fat	920	1430	1.3x10^6
Whole Bone	1500	3300	5.0x10^6

Table 3 Stone properties# for the model

	Stone A (Ca Oxalate)	Stone B (Ca P)
Density (kg/m^3)	1820	1360
Young's Modulus (GPa)	9.05	4.58
Wave Speed (m/s) $	2338	1923

$ calculated from $c=\sqrt{E/\{\rho(1-\upsilon^2)\}}$, where c is the wave speed, E is Young 's modulus and υ is Poisson's ratio (approximated ~ 0.3)
# The stone properties were measured in our laboratory. The stones were supplied from Asahikawa Medical College.

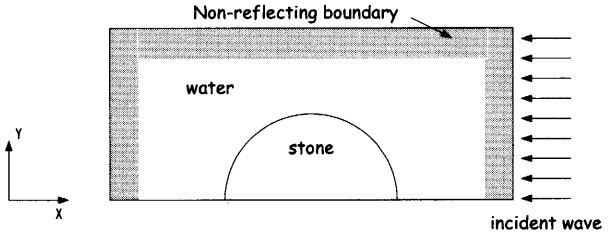

Fig. 2 Computational domain for single impingement

by static compression tests. For convenience, the calcium oxalate and calcium phosphate stones are called the stone *A* and the stone *B*, respectively. The details of the stone properties used are indicated in Table 3.

2.3 Computational domains

For all analyses, only the area around the focal region, where the stone is located, is simulated. The tissue surrounding the stone is modelled as water, because their acoustical properties are similar as shown in Table 2. For simplicity, the shape of the stone is assumed to be perfectly circular with the diameter of 10 mm.

The computational domain of the single impingement analysis is depicted in Fig. 2. Because of symmetry, only the upper half of the section is considered for calculation. In the model, the x-axis is taken as a symmetrical plane. Non-reflecting boundaries are introduced along the computational domain boundaries to prevent stress waves reflected at the model boundaries from reentering the stone model and contaminating the results. The mesh size in the model is in the range of 0.1 mm to 0.25 mm. The size is chosen so that the numerical stability could be guaranteed in the calculation.

2.4 Model parameters

All the models are presented in the rectangular Cartesian coordinates. For the single and double impingement models, two-dimensional solid element is utilized to model both the stone and the water domain whereas for the fragmentation model, a solid element one-point integration is utilized. The stone is regarded as a homogeneous isotropic elastic solid and the water is considered as continuum fluid with bulk modulus of 2.2 GPa, which

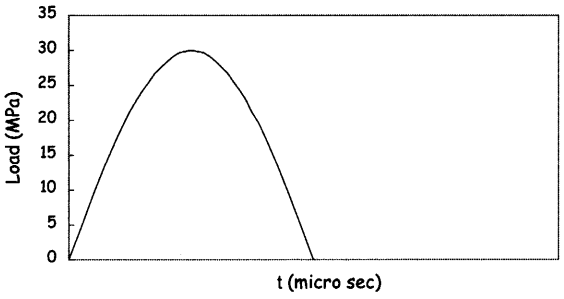

Fig. 3 Short pulse loading for $t=0.5$, 1, 2 and 5 μs

is calculated as a reverse of the isothermal compressibility[10].

To treat the contact between the stone surface and the surrounding water, the calculation uses automatic contact algorithm provided by LS-DYNA for contact of continuum media. The automatic contact algorithm is usually useful for problems in which the contact behavior is initially unknown, thus this algorithm is adopted for the calculation.

The pressure pulse generated by the lithotripter in the focal region is approximated with a half-sine pulse. To study an effect of the incident pulse duration on the stress field evolution inside the stone, pulses with 0.5, 1, 2, and 5 μs duration and amplitude of 30 MPa, as plotted in Fig. 3, are applied from the right hand boundary of the water domain in the single impingement analysis. Two types of stones, namely the stones *A* and *B* are placed in the water domain to observe an effect of the wave speed on the stress field evolution inside the stone.

3. Numerical Results and Discussion

3.1 Single impingement mode

The propagation of the pressure wave in the fluid is shown in Fig. 4. The wave has 0.5 μs duration. The images are captured every 1 μs started from $t=3$ μs. It is seen that, after the incident wave hits the stone as shown in Fig. 4 (d) to (f), some part is reflected back and then propagate toward the domain boundary. When the stress wave travels inside the stone and reaches the stone boundary, some part will be transmitted to the fluid and propagates radially as can be seen in Fig. 4 (g) to (i). Because the wave speed inside the stone is higher than that in the water, this transmitted wave is ahead of the incident wave propagating in the water surrounding the stone. When the stress waves reach the domain boundary, no reflection comes back to the stone as shown in Fig. 4 (j) and (k), because the non-reflecting boundaries are set on the computational domain boundaries.

One typical numerical result on stress field evolution is shown for the single impingement model in Fig. 5. In the figure, normal stress σ_{xx} contours inside the stone *A* subjected to 0.5 μs pressure wave are indicated every 0.6 μs time interval. As shown in Fig. 5 (a) to (e), the

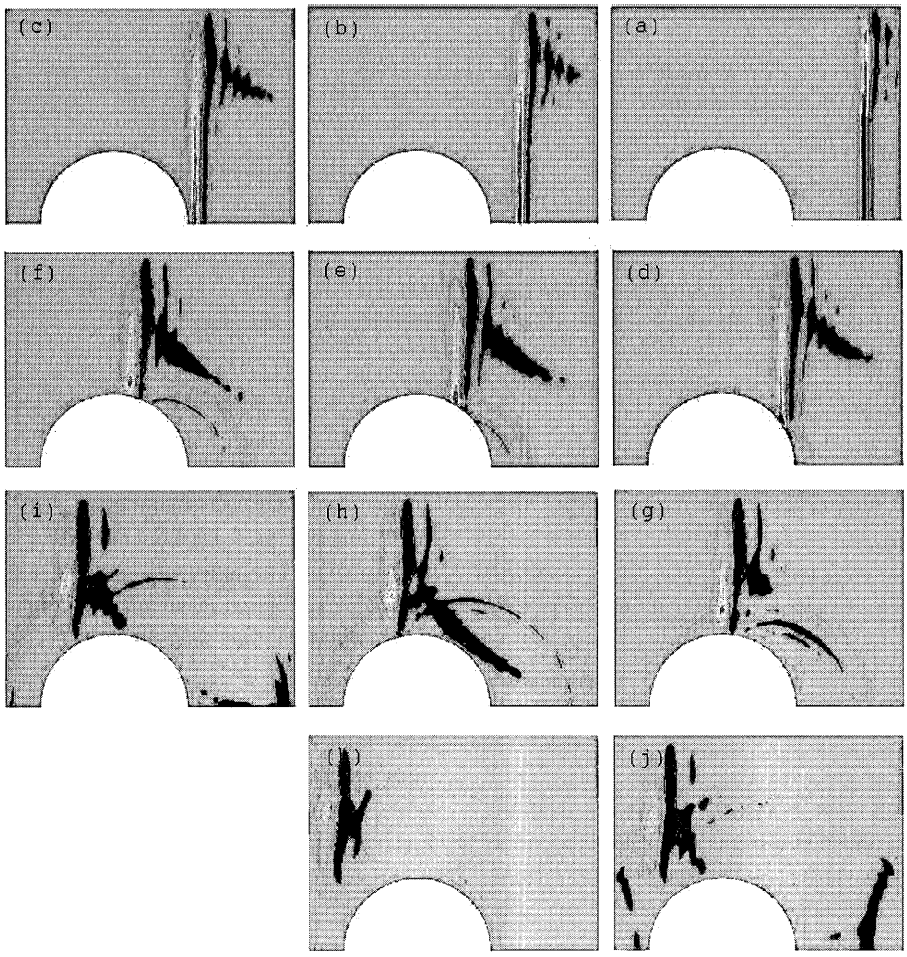

Fig. 4 Pressure wave propagation in the water

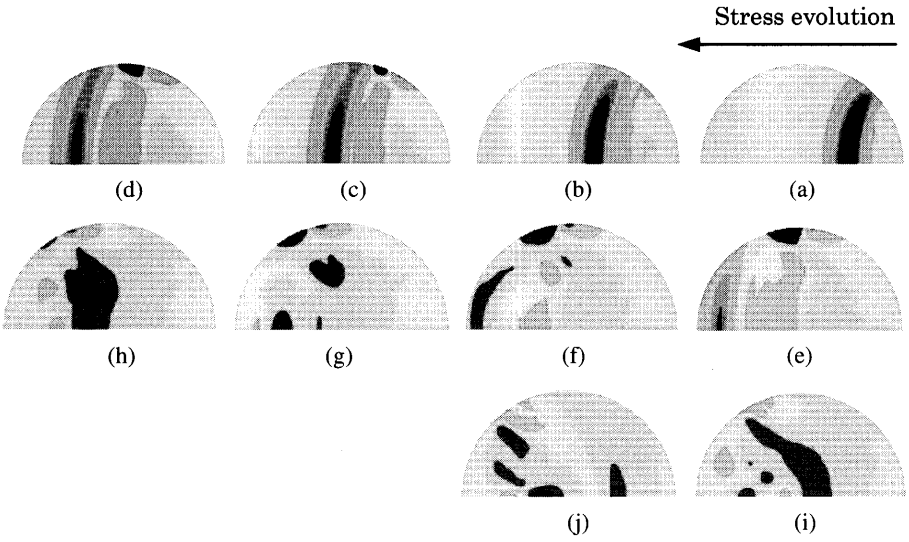

Fig. 5 σ_{xx} evolution inside stone *A* by impingement of 0.5 μs duration pressure wave from the right (6.4 μs after the impingement from the model boundary and 0.6 μs interval)

refracted wave in the circular stone travels to the distal surface. Because of the circular geometry of the stone, reflected waves from the side and the back surface of the stone are focused onto certain locations as shown in Fig. 5 (e) to (h). The reflected tensile stress then propagates to the front surface as shown in Fig. 5 (i) and (j).

The stress evolution inside the stone *B* is similar with that of the stone *A*, except that the stress traveling inside

the stone *B* is shorter than that inside the stone *A*. This results from the fact that the wave speed is higher in the stone *A* than in the stone *B* as indicated in Table 3.

When the stone is subjected to 1 μs and 2 μs stress pulses, and the stress travels toward the back surface boundary, it can be clearly seen how it is reflected and inverted, and then comes back to the front surface of the stone. However, when 5 μs pressure wave is applied to the stone, those stress wave behaviors cannot be clearly identified except the refracted wave that initially propagates to the back surface of the stone. The stress wave length inside the stone, which is comparable with the stone diameter, is the main factor for no clear identification of the stress wave propagation. Because the complex stress wave interaction takes place inside the stone, it is difficult to trace the wave propagation behaviors.

Effects of the loading condition, the stone geometry and its acoustic property on the stress responses inside the circular stone can be studied quantitatively by plotting the stress distribution along the *x*-axis. The maximum compressive stress and the maximum reflected tensile stress distribution therefore have been calculated along the *x*-axis of the stone and are shown in Figs. 6 and 7, respectively.

In Fig. 6, it is seen that for both the stones, the compressive stress magnitude decreases as the wave travels to the back surface of the stone and in general, slightly greater compressive stress is developed in the stone *A* than the stone *B*. However, it does not mean that the stone *A* is more easily fractured than the stone *B*, because the applied stress is one parameter for fracture and the strength of the stone must be considered as another parameter.

Other interesting phenomenon in the maximum compressive stress distribution is that its highest value is not located on the front surface of the stone. It is located inside the stone at certain depth from the front surface. The longer the incident pulse duration, the deeper is the location of the highest stress value.

The reflected tensile stress distribution is plotted as a function of the distance from the stone back surface in

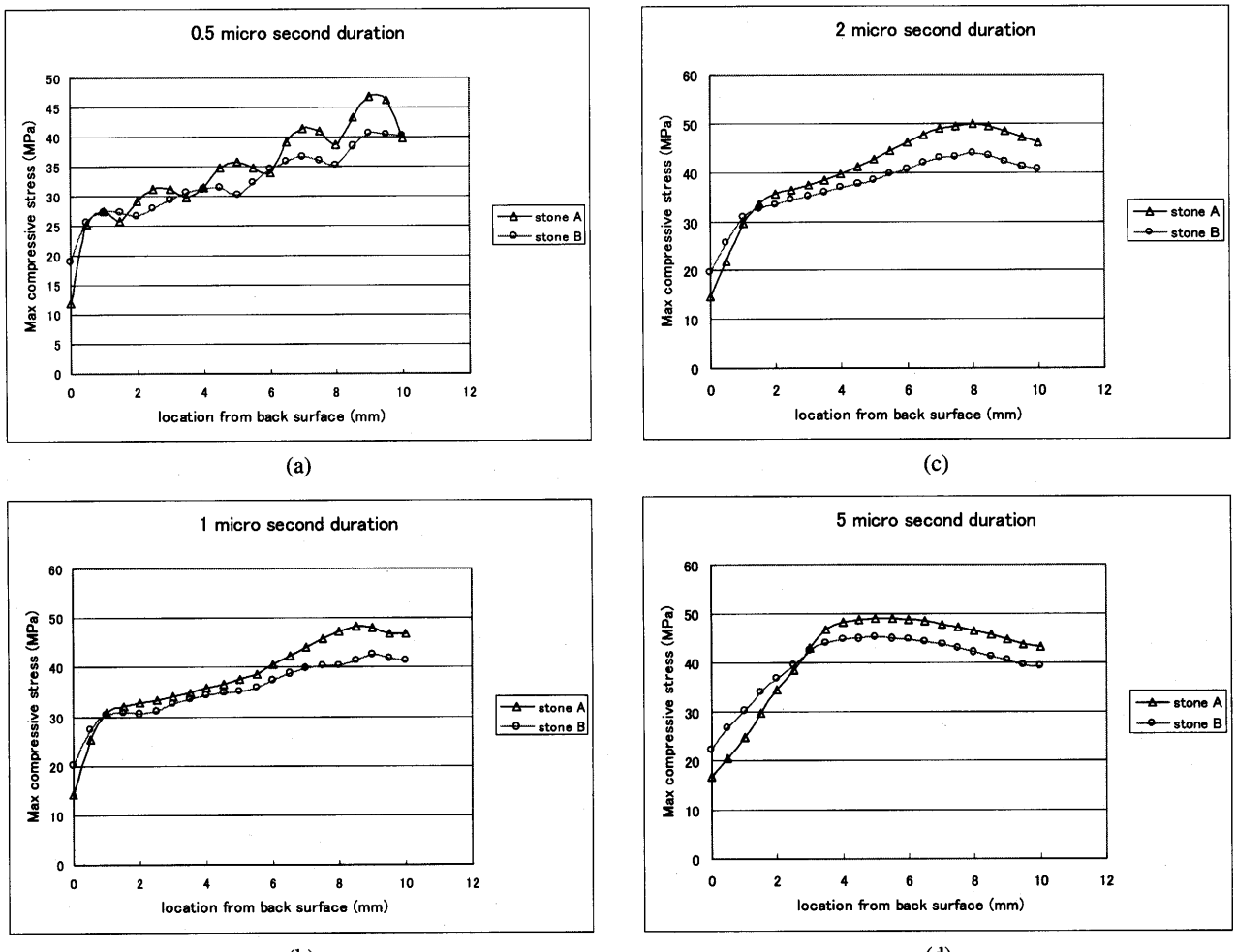

Fig. 6 Maximum compressive stress distribution along axis of symmetry for (a) 0.5 μs, (b) 1 μs, (c) 2 μs and (d) 5 μs incident pulse duration

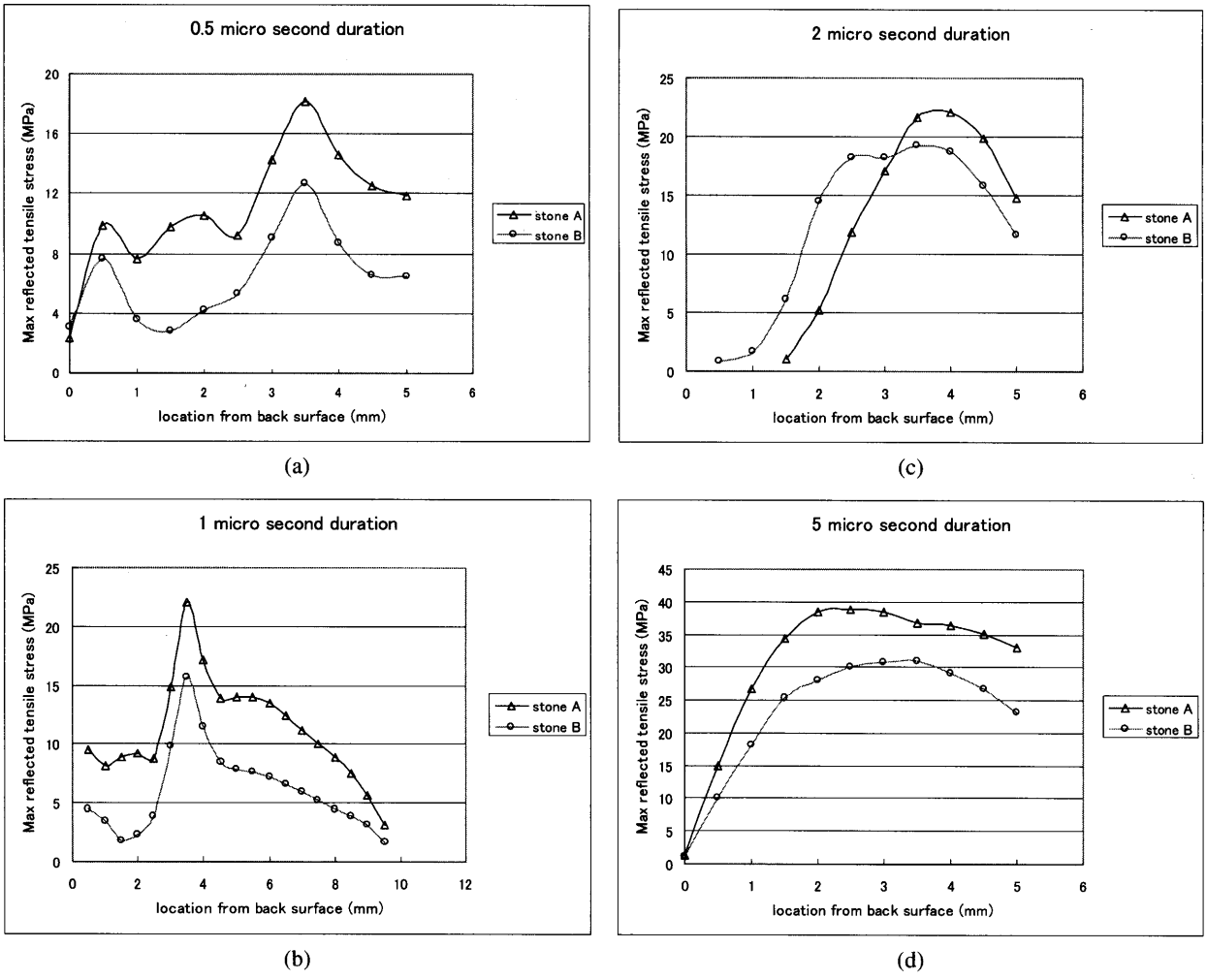

Fig. 7 Maximum reflected tensile stress distribution along axis of symmetry for (a) 0.5 μs, (b) 1 μs, (c) 2 μs and (d) 5 μs incident pulse duration

Fig. 7 (a) – (d). As shown in Fig. 7 (b), the maximum reflected tensile stress is plotted from the back to the front surface of the stone, and the stress fluctuates with the distance from the back surface and reaches the highest value inside the back half of the stone. It is true for all the other cases. Therefore, in Fig. 7 (a), (c) and (d), the curves are plotted only in the back half region.

From Fig. 7, it is seen that the stress is amplified at a certain location as shown by the sharp peak on the curve. This probably reflects a focusing phenomenon of the reflected tensile stresses from the circular boundary of the stone. This phenomenon can be clearly seen in Fig. 5, where the curve peak is located around 3.5 mm distant from the back surface of the stone. Thus, it is suggested that the crack would be likely initiated at this location.

However, if the pulse duration is so long that the wave length is comparable with the stone diameter like the 5 μs incident pulse, the focusing effect is not strong and cannot be seen clearly. This is due to the complex stress interaction between the reflected and the incident wave around the back surface of the stone. It is seen in Fig. 7 (d) that even the focusing effect is not strong, but because of the greater amount of energy transferred into the stone, the impingement pressure with 5 μs pulse duration generates the higher tensile stress inside the stone than the other loading configuration.

3.2 Dual-impingement model

In this model, double pressure waves impinge on the stone simultaneously from different source angles. Combinations of the pulse sources are 1 – 2, 1 – 3, 1 – 4, and 1 – 5 as shown in Fig. 8. In this model, the stone *A* and the pressure pulse with the amplitude of 30 MPa and 1 μs duration are utilized for the analysis.

Time evolution of σ_{xx} contours inside the stone subjected to double incident waves is depicted every 1 μs time interval in Fig. 9. The results are shown in the figure for the 1 – 5 source combination. Both the waves travel toward the center of the stone as shown in Fig. 9 (a) and interact with each other at the center as shown in Fig. 9 (b). Then, high compressive stress is generated. After they pass each other, they are reflected at the stone boundary changing the sign to the tensile stresses as shown in

Fig. 9 (c) to (e). Again, these waves travel toward the center and interact with each other to develop high tensile stresses as shown in Fig. 9 (f). Then, the waves pass the each other again and diverge to become weak as shown in Fig. 9 (g) and (h).

Effect of the source combination on the maximum principle stress inside the stone is examined. The maximum principle stresses generated inside the stone are summarized for different source combinations in Table 4 and the contours are drawn in Fig. 10. The maximum pressure at the surrounding water for each source combination is also presented in the table.

It is seen in this table that the dual impingement does not significantly increase the maximum principal stress inside the stone as compared with the principal stress generated by a single source impingement. However, because the maximum principal stress does not play a main role in the fragmentation of the stone as mentioned in the next section, the further discussion is necessary. For instance, it should be noted that the large high stress area appears in case of the dual impingement as shown in Fig. 11. From Table 4, it can be expected that the 1 – 5 combination in which two pulses are facing each other toward the stone seems to provide better results than other source combination. This combination develops the highest maximum principle stress and has the lowest ratio of the maximum pressure generated in the surrounding water to the maximum principle stress. This means that to reach the same level of the maximum principle stress, lower incident stress can be applied and the lower the ratio, the lower the maximum pressure generated in the surrounding water. Therefore, it will be less risky in the clinical point of view as compared with other source combination.

Examination of this source combination is made concerning the maximum reflected tensile stress distribution along the stone's symmetrical axis in Fig. 11, because this stress is most responsible to the fragmentation as explained in the next section. As a comparison, the corresponding maximum reflected tensile stress distribution

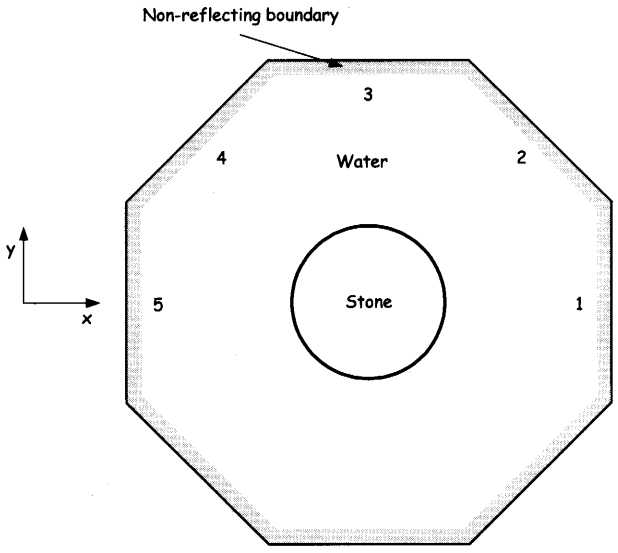

Fig. 8 Double impingement source arrangement

Table 4 Maximum principal stress and maximum pressure generated in the model

Shot Combination	Max S_1 (MPa)	Max Pressure (MPa)	Ratio (Max Pressure/S_1)
Single shot	49.14	44.56	0.91
1 – 2	35.7	75.39	2.11
1 – 3	45.89	43.72	0.95
1 – 4	43.63	40.37	0.93
1 – 5	50.57	42.13	0.83

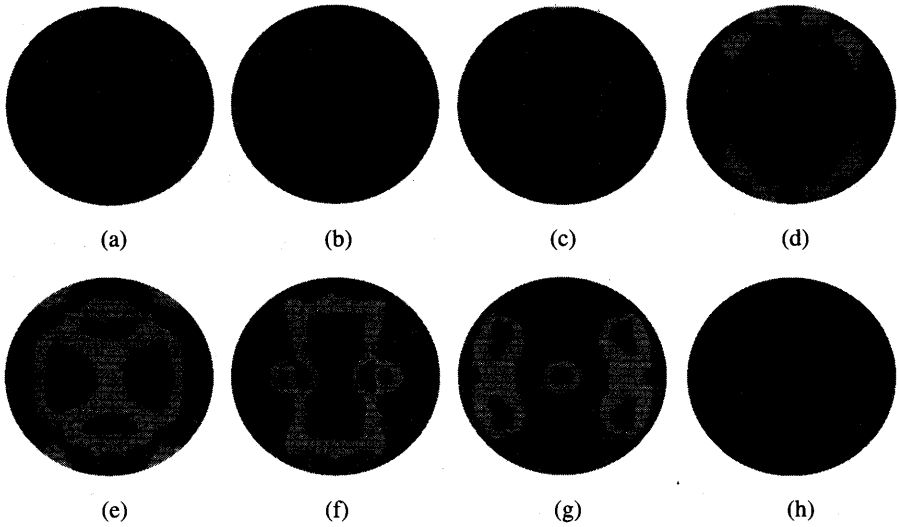

Fig. 9 σ_{xx} evolution inside circular solid of diameter 10 mm due to double incident waves coming from 1 – 5 direction (at interval 1 μs)

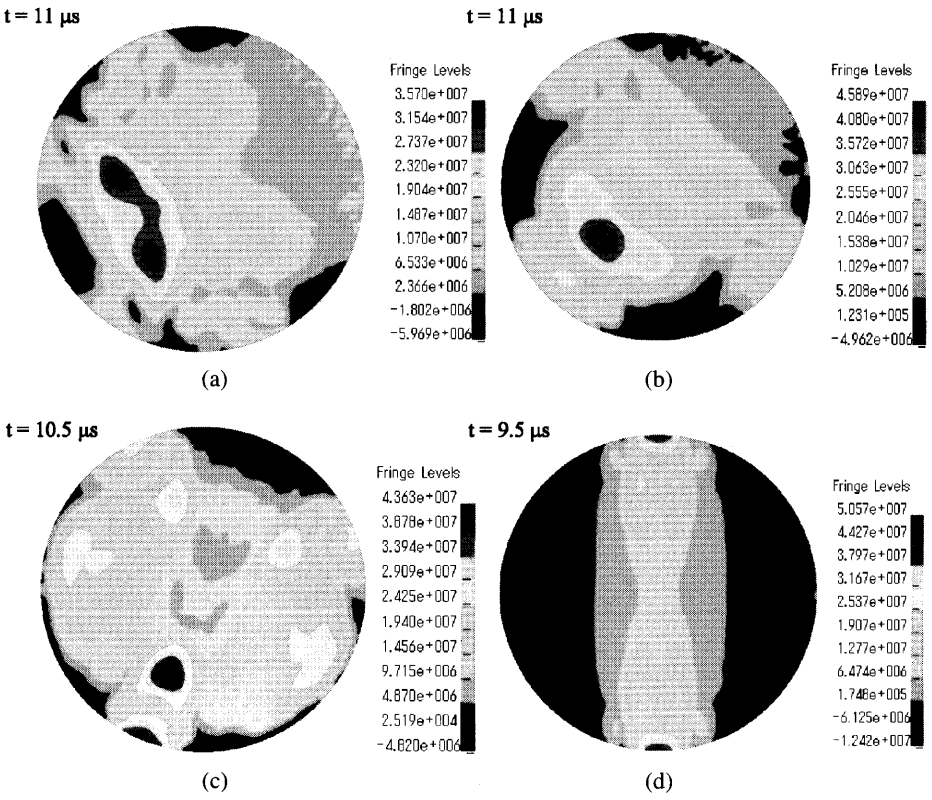

Fig. 10 Maximum principle stress contours due to double incident waves coming from (a) 1 – 2, (b) 1 – 3, (c) 1 – 4, and (d) 1 – 5 directions

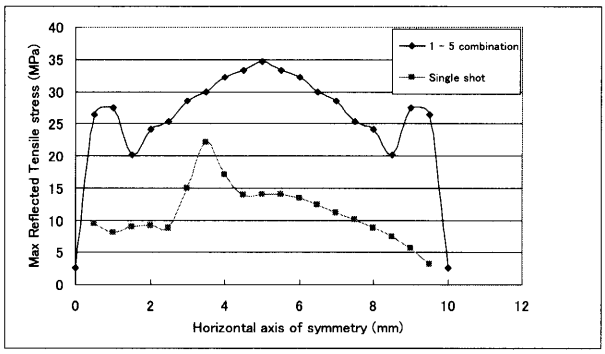

Fig. 11 Maximum reflected tensile stress σ_{xx} distribution in horizontal axis of symmetry

under the single source impingement is also plotted in the figure. It is clearly seen that this dual impingement develops the tensile stress inside the stone one and half times as large as that of the single impingement model. Therefore, in the practice to fragment a kidney stone, a low level of impingement pressure can be used and the risk of kidney tissue injury can be reduced.

The dual-shot lithotripter of 1 – 5 combination has the potential to accelerate stone fragmentation keeping the low risk to the kidney tissue injury. However, even though it is theoretically possible to design such a lithotripter, challenges are necessary to solve several problems in a practical application. One of them is the difficulty to adjust both the wave sources so as to simultaneously hit the stone at the same phase, because the waves reach the stone from different paths of body that probably have different acoustical properties. Therefore, to move the fundamental idea demonstrated in this work to implementation, the special study that deals with those challenges must be carried out.

3.3 Fragmentation model

In Xi et al.[7] experiment, cylindrical plaster disks with various diameters were subjected to the shock wave until fracture. The longitudinal wave speed in the disk is 2 478 m/s and the density is 1 670 kg/m^3. To simulate their experimental work, a 1 mm thick specimen is adopted for the 2D analysis. Therefore, some measures taken in the single impingement model described above are adopted in the fragmentation model and the computational domain of this model is similar to the model depicted in Fig. 2, except that the current model has 1 mm thickness in z-direction. Because of the symmetry, only an upper half of the model is considered for calculation. In the model, the x-axis is taken as a symmetrical plane. The mesh size in the model is around 0.25 mm. The size is decided by considering both the numerical stability and the computation efficiency in the calculation.

Tuler and Butcher criterion is adopted for this simulation. They introduced a general criterion for time-dependent dynamic fracture initiation by using the con-

cept of cumulative damage[11]. The criterion is expressed by the following equation:

$$\int_0^{t_f} (\sigma_1 - \sigma_0)^2 dt \geq K_f \qquad (1)$$

for $\sigma_1 \geq \sigma_0 \geq 0$, where σ_1 is the maximum principal stress, σ_0 is a specified threshold stress, t_f is time for fracture and K_f is the stress impulse for failure.

According to this formula, stress below the threshold value does not contribute to fracture even if its acting duration is very long. Fracture is recognized by the program when the stress action in any elements exceeds K_f. Because the dynamic strength of the specimen is unknown, the threshold stress and the stress impulse for fracture are taken as the following trial values in the analysis: $\sigma_0 = 6.42$ MPa, $K_f = 1.0\,\text{MPa}^2 \cdot \mu\text{s}$. Assuming that σ_1 is a step function, we can interpret K_f as the meaning that the element breaks if σ_1 exceeds σ_0 by 1 MPa for at least 1 μs.

The fragmentation result is shown in Fig. 12 when the stone is subjected to the impingement pressure with 1 μs pulse duration and the amplitude of 15 MPa. It is seen that small fracture takes place in the back surface of the stone. However, this crack does not propagate further over the analysis time up to 30 μs.

When the pressure with the higher amplitude of 18 MPa is applied to the stone, the crack pattern is significantly different from the previous result as seen in Fig. 13. After the reflected tensile wave comes to the location at the time of 11.75 μs, the first crack is initiated at the horizontal axis, and soon after the first crack initiation, another vertical crack is initiated at the time of 12.25 μs. Then, both the cracks propagate horizontally to the back boundary, and vertically until the stone finally breaks into three pieces.

However, the careful observation of crack behaviors after the time of 15.75 μs in Fig. 13 shows that a new crack appears at the back surface and propagates to coalesce with the former horizontal crack. From the above phenomena, it can be concluded that the maximum principal stress is generated at the back surface of the stone, but it is not responsible to the catastrophic stone fragmentation. It should be also noted that the rather high tensile stress appears at several microseconds after the reflected tensile stresses are focused onto a certain location inside the stone, and takes a major role for the stone fragmentation. Therefore, if the applied pressure is increased, a crack would likely be initiated and extended inside the stone due to the focusing effect of reflected tensile stresses. On the contrary, the maximum principal stress lives very

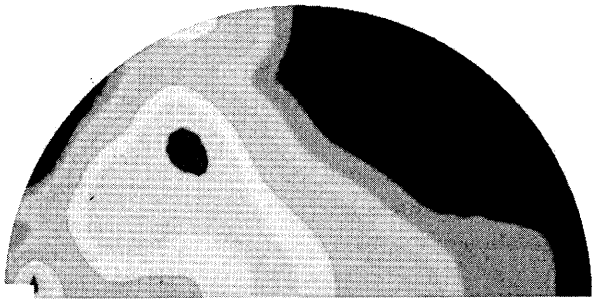

Fig. 12 Fragmentation result after application of 15 MPa pulse

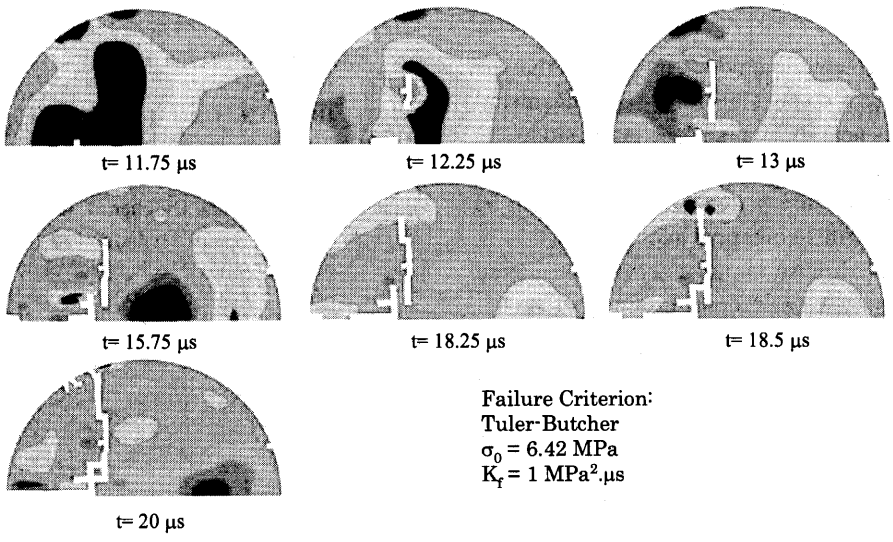

Fig. 13 Fragmentation result after application of 18 MPa pulse

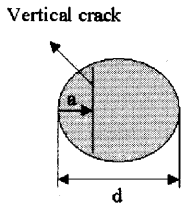

	Experiment	Numerical Model
a/d	0.31	0.35

Fig. 14 Relative position of the vertical crack measured from the back surface of cylindrical disks

shortly at the back surface, and can not play a major role for the final fragmentation of the stone.

The fracture pattern estimated by the simulation as shown in Fig. 13 is in excellent agreement with the experimental results by Xi et al.[7] To compare the results more quantitatively, the relative position of the vertical crack measured from the back surface are calculated. The results are given in Fig. 14. It is shown that the relative position of vertical crack in the numerical model is almost similar with the experimental one.

4. Conclusions

Some numerical calculations have been carried out in this work with aim to study the mechanism of kidney stone fragmentation by lithotripter shock wave. The following conclusions are obtained:

1. Pulse duration of the incident wave and stone acoustic properties play a significant role in the stress behaviors inside the stone, such as the location of the maximum reflected tensile stress.

2. If the stone has a concave boundary, the reflected waves will be converged at a certain location and produce higher stress magnitude. Thus, the crack is likely initiated at this location.

3. From the fragmentation model, it is shown that the reflected tensile stress is responsible for the spalling mechanism, which occurs near the rear surface of the stone.

4. Although fracture criterion used in this simulation is rather simple, the fracture pattern of the stone can be precisely simulated by this numerical analysis.

5. The use of dual pulse impingement is considered for the patient-friendly kidney stone fragmentation, because it develops high tensile stress inside the stone one and a half times as large as that of the single impingement. Therefore, low impingement pressure can be used for kidney stone fragmentation, which can reduce the risk of the kidney tissue injury.

References

(1) Zhu, S., Cocks, F.H., Preminger, G.M. and Zhong, P., The Role of Stress Waves and Cavitation in Stone Comminution in Shock Wave Lithotripsy, Ultrasound in Medicine & Biology, Vol.28, No.5 (2002), pp.661–671.

(2) Cleveland, R.O., Bailey, M.R., Fineberg, N., Hartenbaum, B., Lokhandwalla, M., McAteer, J.A. and Sturtevant, B., Design and Characterization of a Research Electrohydraulic Lithotripter Patterned after the Dornier HM3, Review of Scientific Instruments, (2000), pp.1–27.

(3) Crum, L.A., Cavitation Microjets as a Contributory Mechanisms for Renal Calculi Disintegration in ESWL, The Journal of Urology, Vol.140 (1988), pp.1587–1590.

(4) Chaussy, C., Brendel, W. and Schmiedt, W., Extracorporeally Induced Destruction of Kidney Stones by Shock Waves, Lancet (1980), pp.1265–1268.

(5) Chuong, C.J., Zhong, P., Arnott, H. and Preminger, G.M., Stone Damage Modes during Piezoelectric Shock Wave Delivery, edited by Lingeman, J.E. and Newman, D.M., Shock Wave Lithotripsy II, (1989), pp.103–106, Plenum Press, New York.

(6) Khan, S.R., Hackett, R.L. and Finlayson, B., Morphology of Urinary Stone Particles Resulting from ESWL Treatment, The Journal of Urology, Vol.136 (1986), pp.1367–1372.

(7) Xi, X. and Zhong, P., Dynamic Photoelastic Study of the Transient Stress Field in Solid during Shock Wave Lithotripsy, Journal of Acoustical Society of America, Vol.109, No.3 (2001), pp.1226–1239.

(8) Chuong, C.J., Zhong, P. and Preminger, G.M., Acoustic Property Measurement of Renal Calculi (abstract), The Journal of Urology, Vol.145 (1991), p.254A.

(9) Duck, F.A, Physical Properties if Tissue: A Comprehensive Reference Book, (1990), Academic Press, London.

(10) Lide, D.R., CRC Handbook of Chemistry and Physics, 78th Edition, (2003), pp.6–140, CRC Press, Boca Raton, Florida.

(11) Tuler, F.R. and Butcher, B.M., A Criterion for the Time Dependence of Dynamic Fracture, International Journal of Fracture Mechanics, Vol.4, No.4 (1968), pp.431–437.